

RESEARCH

Open Access



Quantitative hypoxia mapping using a self-calibrated activatable nanoprobe

Xin Feng^{1,2}, Yuhao Li³, Shiyuan Zhang¹, Changjian Li⁴ and Jie Tian^{1,4,5,6*} 

Abstract

Hypoxia is a distinguished hallmark of the tumor microenvironment. Hypoxic signaling affects multiple gene expressions, resulting in tumor invasion and metastasis. Quantification of hypoxic status although challenging, can be useful for monitoring tumor development and aggressiveness. However, hypoxia-independent factors such as nonspecific binding and heterogenous probe delivery considerably influence the probe signal thereby disabling reliable quantitative imaging *in vivo*. In this study, we designed a self-calibrated activatable nanoprobe Cy7-1/PG5-Cy5@LWHA that specifically detects nitroreductase activity upregulated in hypoxic tumor cells. Dual fluorescence emission of the nanoprobe enables ratiometric calibration and eliminates the target-independent interference. In orthotopic and metastatic breast cancer mouse models, Cy7-1/PG5-Cy5@LWHA demonstrated remarkable hypoxia sensing capability *in vivo*. Moreover, ratiometric processing provided quantitative hypoxia assessment at different tumor developmental stages and facilitated tumor burden assessment in the metastatic lymph nodes. Therefore, our study demonstrates that ratiometric imaging of Cy7-1/PG5-Cy5@LWHA can be a prospective noninvasive tool to quantitatively monitor tumor hypoxia, which would be beneficial for investigating the fundamental role of hypoxia in tumor progression and for evaluating response to novel anti-hypoxia therapeutics. Furthermore, successful detection of metastatic lymph nodes with the proposed imaging approach illustrates its potential clinical application in assessing lymph node status during surgery.

Keywords: Hypoxia, Ratiometric imaging, Quantitative, Breast cancer

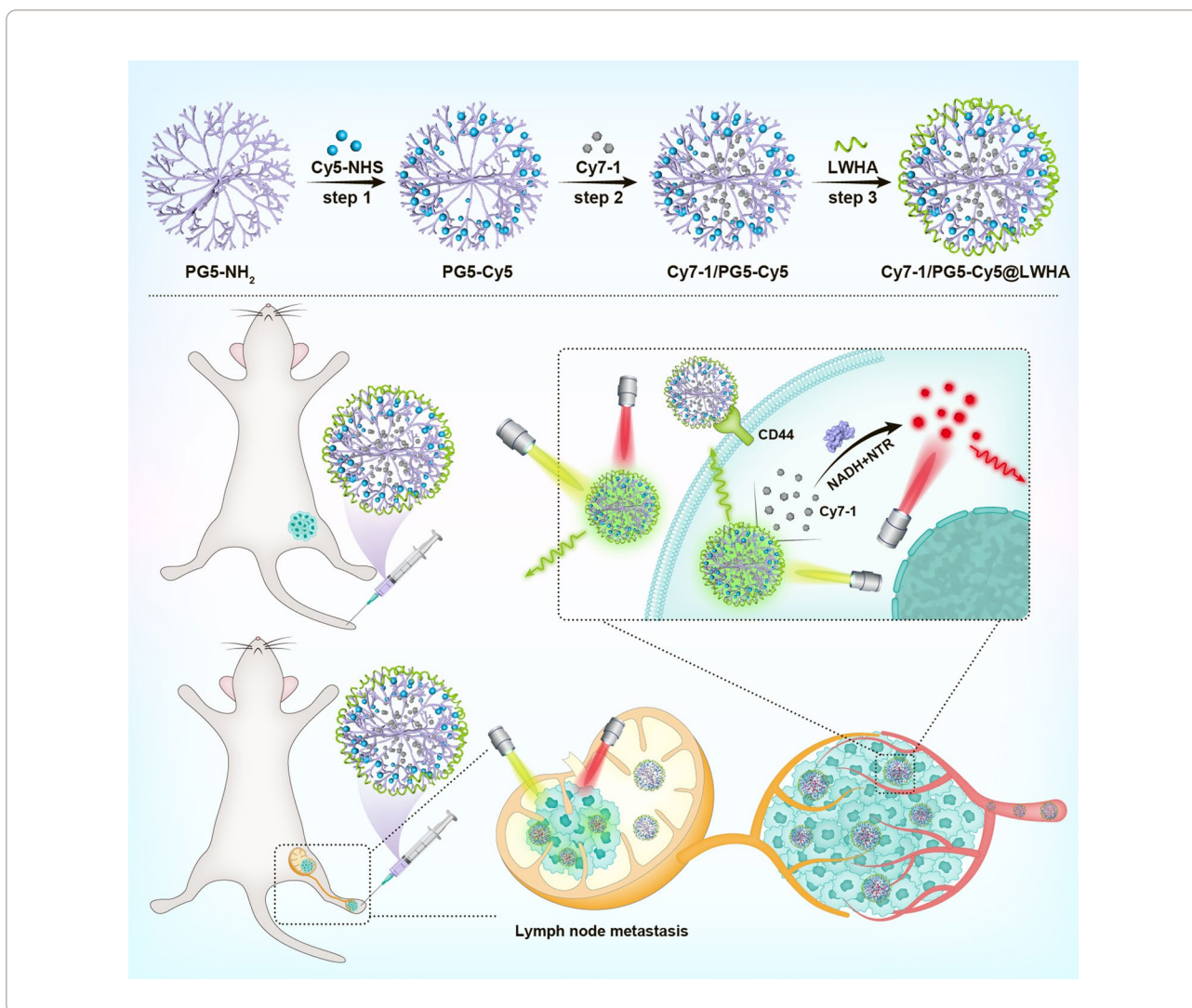
Graphical Abstract

*Correspondence: jie.tian@ia.ac.cn

¹ CAS Key Laboratory of Molecular Imaging, Beijing Key Laboratory of Molecular Imaging, the State Key Laboratory of Management and Control for Complex Systems, Institute of Automation, Chinese Academy of Sciences, Beijing 100190, China
Full list of author information is available at the end of the article



© The Author(s) 2022. **Open Access** This article is licensed under a Creative Commons Attribution 4.0 International License, which permits use, sharing, adaptation, distribution and reproduction in any medium or format, as long as you give appropriate credit to the original author(s) and the source, provide a link to the Creative Commons licence, and indicate if changes were made. The images or other third party material in this article are included in the article's Creative Commons licence, unless indicated otherwise in a credit line to the material. If material is not included in the article's Creative Commons licence and your intended use is not permitted by statutory regulation or exceeds the permitted use, you will need to obtain permission directly from the copyright holder. To view a copy of this licence, visit <http://creativecommons.org/licenses/by/4.0/>. The Creative Commons Public Domain Dedication waiver (<http://creativecommons.org/publicdomain/zero/1.0/>) applies to the data made available in this article, unless otherwise stated in a credit line to the data.



Introduction

Hypoxia, resulting from the rapid proliferation of cancer cells and poor tumor vasculature, is one of the most pervasive features of solid tumors [1]. In order to adapt to the oxygen-deprived microenvironment, hypoxia-inducible transcription factor (HIF-1) is activated in cancer cells, which subsequently upregulates genes associated with metabolic alteration, cell migration, metastasis, and treatment resistance [2–5]. Therefore, hypoxia is often identified as an indicator of tumor aggressiveness and poor prognosis. Recently, it has also been reported that metastatic tumors exhibit the same hypoxia signatures as the primary tumor [6, 7]. In this context, hypoxia imaging is beneficial for evaluating tumor malignancy and can be helpful for identifying tumor metastasis as well.

Over the past decades, nitroreductase (NTR) has been identified as a biomarker for hypoxia [8–10]. It has been reported that NTR activity is elevated in hypoxic tumors [8], ischemic myocardial tissue [9], and bacterial infections [10]. NTR catalyzes the reduction of nitro compounds to amines in the presence of NAD(P)H [11]. Based on this reaction, multiple NTR-activatable fluorescence probes have been designed for tumor hypoxia imaging, most of them are based on quinones or nitroaromatic compounds [12–17]. Activatable probes have greatly improved the imaging specificity since fluorescence signal is only turned on in hypoxic tumor cells. However, hypoxia assessment *in vivo* remains to be challenging, since vascular abnormalities associated with hypoxia [18, 19] often affect probe delivery, leading to heterogeneous local probe concentration. As a result,

in vivo probe signal cannot reliably reflect the NTR activity, thus hinders the accurate hypoxia quantification.

Herein, we designed a self-calibrated NTR activatable nanoprobe Cy7-1/PG5-Cy5@LWHA that enables accurate hypoxia imaging. Activatable fluorescent reporter Cy7-1 was used to sense the NTR activity [15], and an “always-on” Cy5 fluorophore was employed as an internal reference to account for heterogeneity in probe delivery. Two fluorophores were incorporated together through the poly(amidoamine) dendrimer (5th generation, PG5), and the nanoconjugate was modified with low molecular weight hyaluronic acid (LWHA, molecular weight 5 kDa) to enable cell internalization through CD44. Our results demonstrate that ratiometric imaging of Cy7-1/PG5-Cy5@LWHA enabled quantitative assessment of hypoxia in vivo in orthotopic and metastatic breast cancer models. In vivo imaging results agree with the findings of ex vivo semi-quantitative techniques including immunofluorescence and qPCR. The present study delivers a noninvasive tool to quantify the extent of tumor hypoxia, which would facilitate the study of tumor biology and the development of anti-hypoxia strategies. The successful detection of metastatic lymph node (LN) using this approach further suggests its potential use in LN assessment during surgery.

Results

Design, synthesis, and characterization of the self-calibrated activatable nanoprobe

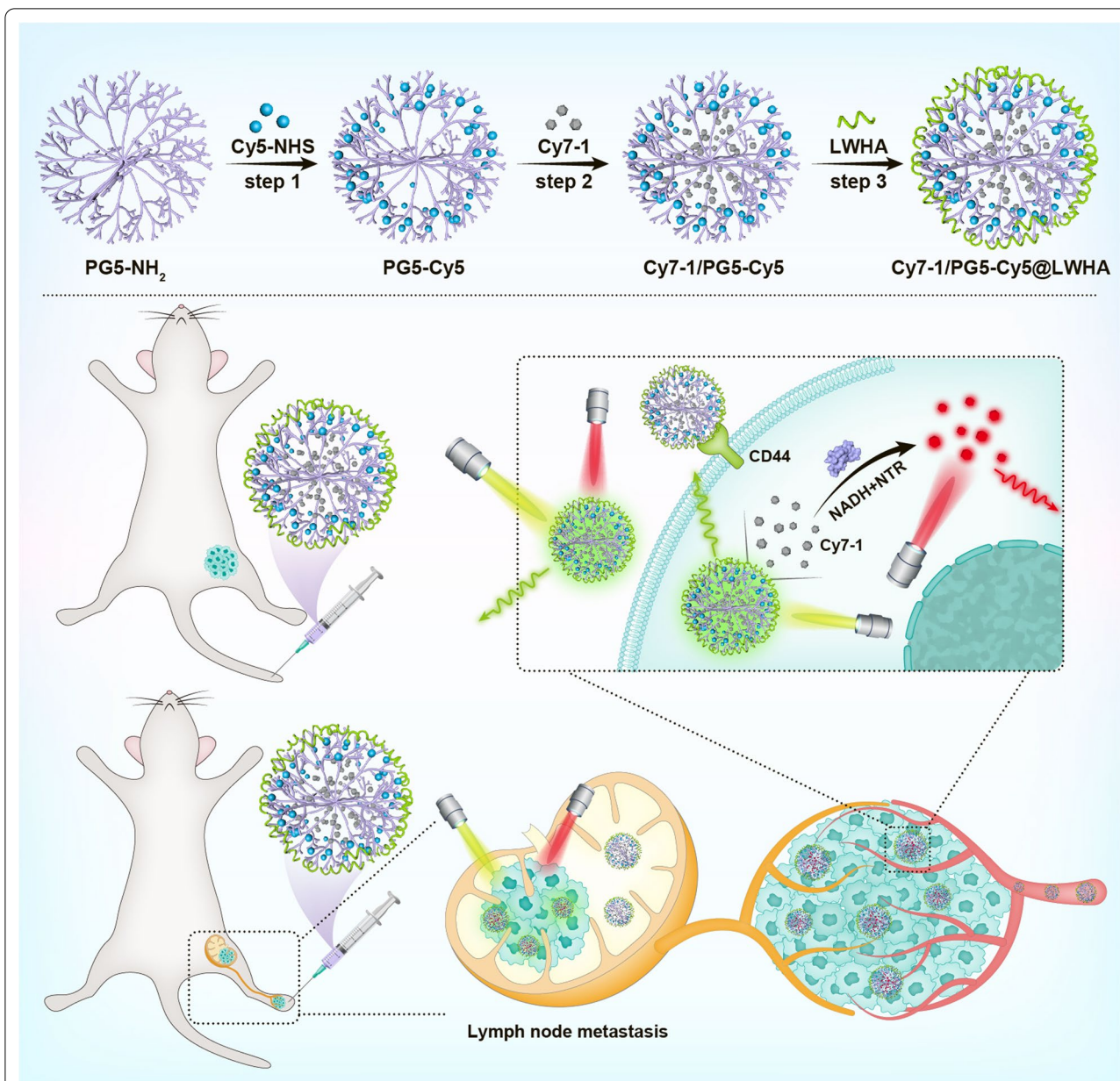
Hypoxia-activatable NIR dye Cy7-1, an “always-on” fluorophore Cy5, and LWHA were incorporated together using PG5 to form a self-calibrated activatable nanoprobe Cy7-1/PG5-Cy5@LWHA. PG5 was selected as the nanocarrier because of its consistent nanometer size, globular shape, and polyfunctional dendrimer surface [20]. Synthesis route, structure and function of the nanoprobe are illustrated in Scheme 1. Briefly, Cy5-NHS was covalently conjugated to the peripheral amino groups on PG5, with a labeling rate of 2% (PG5-Cy5). After purification, hydrophobic Cy7-1 was encapsulated in the internal cavities of PG5-Cy5 at a loading rate of 8% (Cy7-1/PG5-Cy5). The CD44 targeting group LWHA [21] was coated on the surface of Cy7-1/PG5-Cy5 to form Cy7-1/PG5-Cy5@LWHA. After purification, Cy7-1/PG5-Cy5@LWHA was characterized using Fourier transform infrared spectroscopy (Figure S1). The absorption spectra of Cy7-1, Cy5, and Cy7-1/PG5-Cy5@LWHA are presented in Fig. 1a. Cy7-1/PG5-Cy5@LWHA (black curve) showed two distinct absorption peaks around 620 nm and 770 nm, indicating the successful labeling of Cy5 and encapsulation of Cy7-1, respectively. Prior to LWHA modification, the zeta potential of Cy7-1/PG5-Cy5 was approximately +37.4 mV, which could lead to

cell toxicity and low retention time in circulation [22]. Negatively charged LWHA neutralized the cationic surface charge and shifted the zeta potential to -31.1 mV (Fig. 1b). The hydrodynamic size of Cy7-1/PG5-Cy5@LWHA was 146.7 nm. Transmission electron microscopy (TEM) revealed that the nanoprobe were well-separated spheres with a size of approximately 108 nm (Fig. 1c).

NTR response of the nanoprobe

The fluorescence emission spectra of Cy7-1/PG5-Cy5@LWHA are presented in Fig. 2a. Under normal physiological conditions (37 °C, pH 7.4), the emission peak was located around 666 nm when excited at 635 nm. No obvious emission was detected when excited at 769 nm. To investigate the NTR response of the nanoprobe in vitro, 0.5 µg/ml NTR and 0.35 mg/ml NADH in Tris buffer were used [15]. After incubating with the NTR/NADH solution for 5 min at 37 °C, Cy7-1/PG5-Cy5@LWHA exhibited a distinct emission peak around 785 nm when excited at 769 nm, indicating that Cy7-1 was reduced to fluorescent Cy7. The fluorescence intensity at 785 nm was 41-fold that measured without NTR (Fig. 2a). To explore whether encapsulation of Cy7-1 could affect its NTR sensitivity, free Cy7-1 was incubated with the above-mentioned NTR/NADH solution under the same conditions. Spectroscopy measurements showed that the fluorescence intensity of free Cy7-1 increased 51-fold after incubation (Figure S2). Thus, encapsulation of Cy7-1 slightly reduced NTR sensitivity, yet the nanoprobe still exhibited sufficient signal enhancement in response to NTR. Conversely, Cy5 fluorescence remained unchanged after the addition of NTR (Fig. 2a), and was linearly correlated with the nanoprobe concentration (Fig. 2b, c). Therefore, Cy5 fluorescence was used as an internal reference to eliminate the effect of local probe concentration on NTR quantification.

To validate our ratiometric approach to quantify NTR, different concentrations of Cy7-1/PG5-Cy5@LWHA were incubated with NTR solutions ranging from 0 to 1.5 µg/ml in a 96-well plate and imaged with the IVIS imaging system. As shown in Fig. 2d, even though Cy7-1 fluorescence (I_{800}) increased with NTR concentration (top to bottom), the nanoprobe concentration also affected the signal intensity (left to right). This mimics the in vivo situation where the nanoprobe concentration in the tumor region is heterogeneous due to the differences in vasculature, interstitial pressure, and other physiological factors that may affect probe delivery. The signal enhancement of I_{800} is a combined result of NTR activity and probe accumulation. Thus, I_{800} alone cannot reliably reflect the NTR level. As shown in Fig. 2e, fluorescence of the internal reference Cy5 (I_{680}) was unaffected by NTR (top to bottom), directly reflecting the nanoprobe

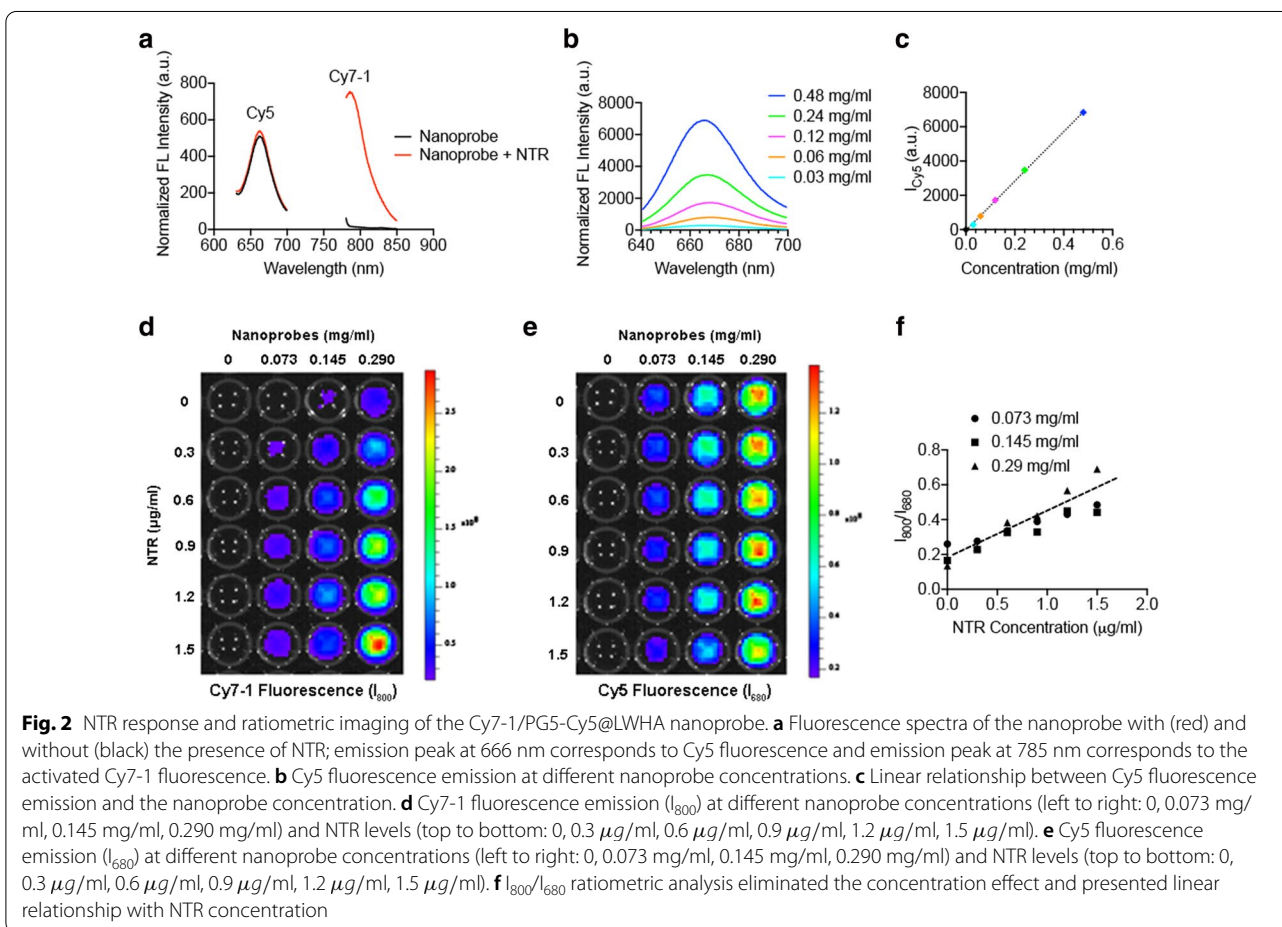
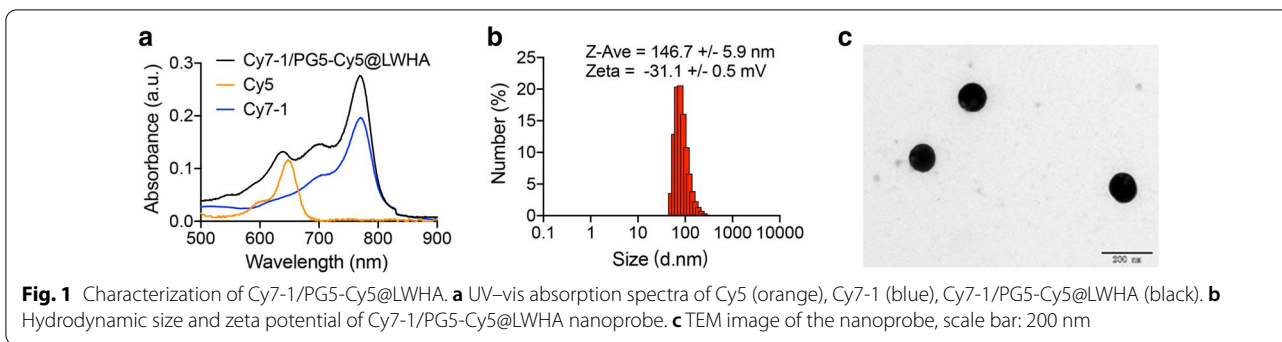


Scheme 1 Synthesis route, structure and function of the self-calibrated activatable nanoprobe Cy7-1/PG5-Cy5@LWHA. Top: synthesis route and structure of Cy7-1/PG5-Cy5@LWHA. Bottom: In vivo imaging of Cy7-1/PG5-Cy5@LWHA allowed for quantitative hypoxia imaging in orthotopic and LN metastatic breast cancer models. “Always-on” Cy5 in the nanoprobe is used to monitor probe accumulation, and Cy7-1 in the nanoprobe is used to sense NTR activity in the hypoxic tumor cells. The nanoprobe was administered through tail-vein injection in orthotopic tumor model and through intratumoral injection in LN metastatic models

concentration. After ratiometric calibration, the signal ratio (I_{800}/I_{680}) showed a good linear relationship with the NTR concentration, and was independent of the nanoprobe concentration (Fig. 2f). Thus, ratiometric calibration of the nanoprobe eliminated the concentration effect and demonstrated an outstanding capability for NTR quantification.

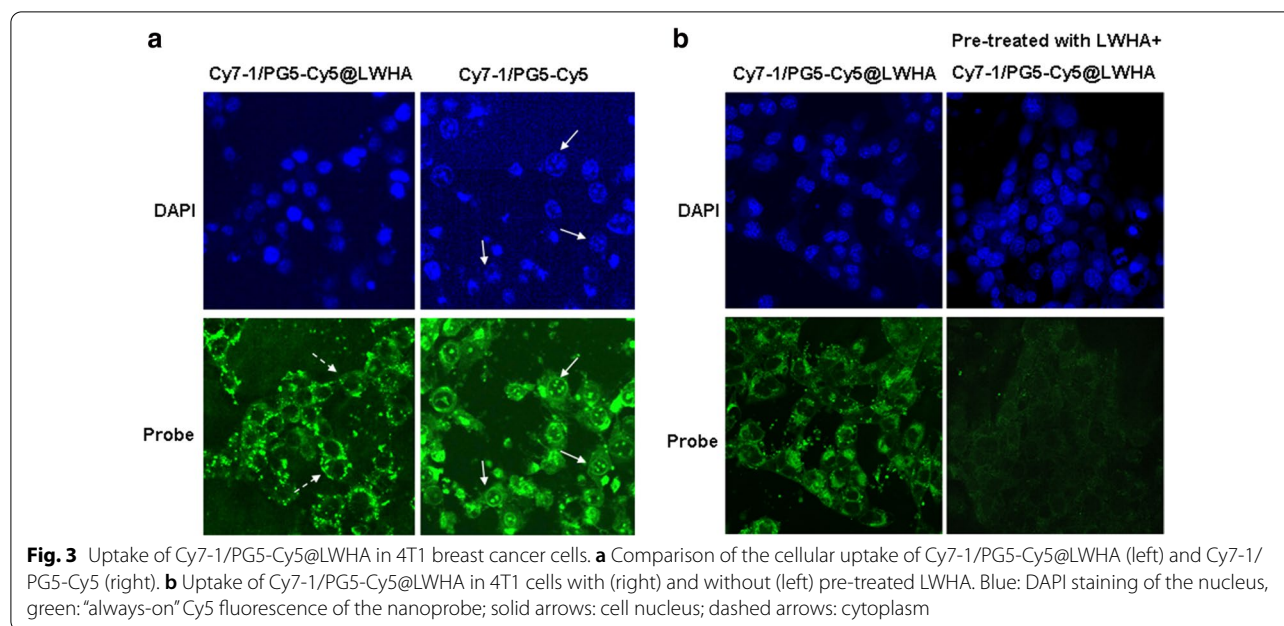
Cellular uptake of the nanoprobe

Previous studies have shown that elevated NTR activity is a distinguished feature of hypoxic tumor microenvironment, and is found inside hypoxic cancer cells [23]. Thus, to allow efficient hypoxia imaging, the nanoprobe needs to enter cancer cells to react with NTR. Previous studies have shown that LWHA can efficiently target CD44



receptor overexpressed on cancer cells and can be internalized via CD44-mediated endocytosis [21]. To explore the cellular uptake pattern of Cy7-1/PG5-Cy5@LWHA, CD44⁺ 4T1 cells were incubated with the nanoprobes (0.05 mg/ml) for 4 h and fluorescence was subsequently observed with a confocal microscope. To investigate the effect of LWHA modification, cells were also incubated with Cy7-1/PG5-Cy5 (0.05 mg/ml) and imaged under the same conditions. As shown in Fig. 3a, both Cy7-1/

PG5-Cy5@LWHA and Cy7-1/PG5-Cy5 were taken up by 4T1 cells. Cy7-1/PG5-Cy5@LWHA accumulated in the cell cytoplasm (white dashed arrows), while Cy7-1/PG5-Cy5 entered the cell nucleus (white solid arrows). The different intracellular distributions of the two nanoprobes could be explained by their opposing surface charges and different internalization mechanisms. Cationic Cy7-1/PG5-Cy5 entered the cell and nucleus via nonspecific electrostatic interactions, as reported for other cationic



probes. On the other hand, anionic Cy7-1/PG5-Cy5@LWHA entered the cells through CD44 receptors and remained within the cytoplasm upon internalization. Although both nanoprobe were able to get into the cancer cells, it has been reported that cationic probes are prone to cytotoxicity. Therefore, we performed an MTT assay to further investigate the biocompatibility of the two nanoprobe. As shown in Additional file 3: Figure S3, Cy7-1/PG5-Cy5@LWHA exhibited good biocompatibility, while Cy7-1/PG5-Cy5 showed significant cytotoxicity.

To further confirm the internalization mechanism of Cy7-1/PG5-Cy5@LWHA, 4T1 cells were incubated with free LWHA to block CD44 and then incubated with Cy7-1/PG5-Cy5@LWHA. As presented in Fig. 3b, cellular uptake of Cy7-1/PG5-Cy5@LWHA significantly decreased after CD44 receptors were blocked. Overall, our results demonstrated that the Cy7-1/PG5-Cy5@LWHA nanoprobe entered CD44⁺ breast cancer cells through CD44-mediated endocytosis, and later localized to the endolysosomal compartments in the cytoplasm.

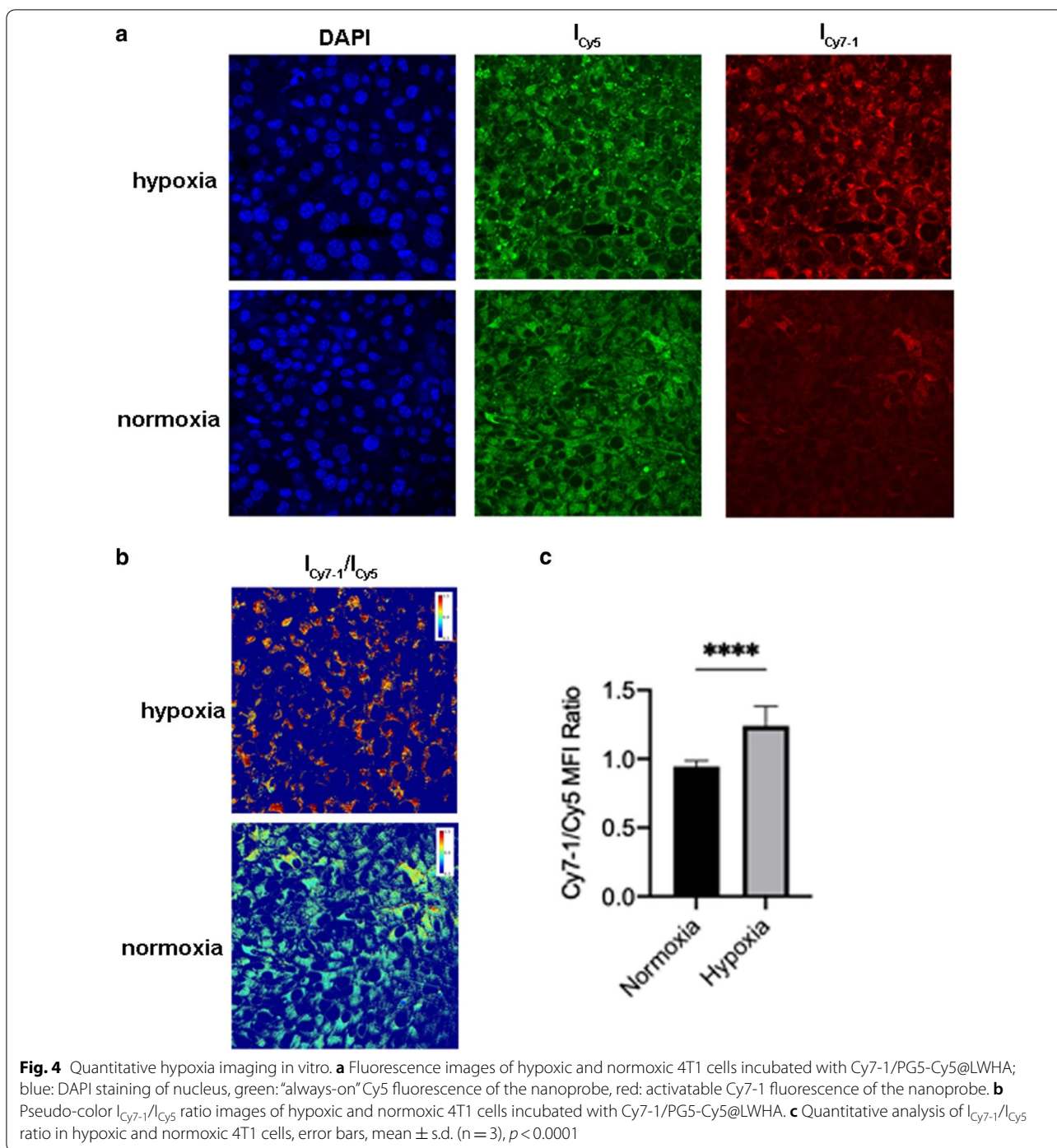
Hypoxia imaging in vitro

To test the performance of Cy7-1/PG5-Cy5@LWHA with respect to imaging hypoxia in living-cell assays, cobalt chloride (CoCl₂) was used to induce hypoxia in 4T1 cells [24]. Hypoxic and normoxic cells were incubated with 0.05 mg/ml Cy7-1/PG5-Cy5@LWHA for 4 h and imaged under a confocal microscope. As shown in Fig. 4a, the Cy5 fluorescence was comparable between hypoxic and control cells, indicating that hypoxia did not affect the cellular uptake or intracellular localization

of the nanoprobe. In contrast, Cy7-1 fluorescence intensity remarkably increased in hypoxic cells, suggesting the successful activation of the nanoprobe by NTR. We believe that the nanoprobe first underwent conformational change in the low pH environment in lysosomes [25]. Cy7-1 was then released and reacted with NTR. The pseudo color images in Fig. 4b showed notably higher $I_{\text{Cy7-1}}/I_{\text{Cy5}}$ ratio in the cytoplasm of CoCl₂-treated cells, demonstrating the sensitivity of the ratiometric approach for detecting hypoxia. Quantitative analysis of three independent batches of cells confirmed that the $I_{\text{Cy7-1}}/I_{\text{Cy5}}$ ratio was significantly higher in hypoxic cells than in normoxic cells ($p < 0.0001$).

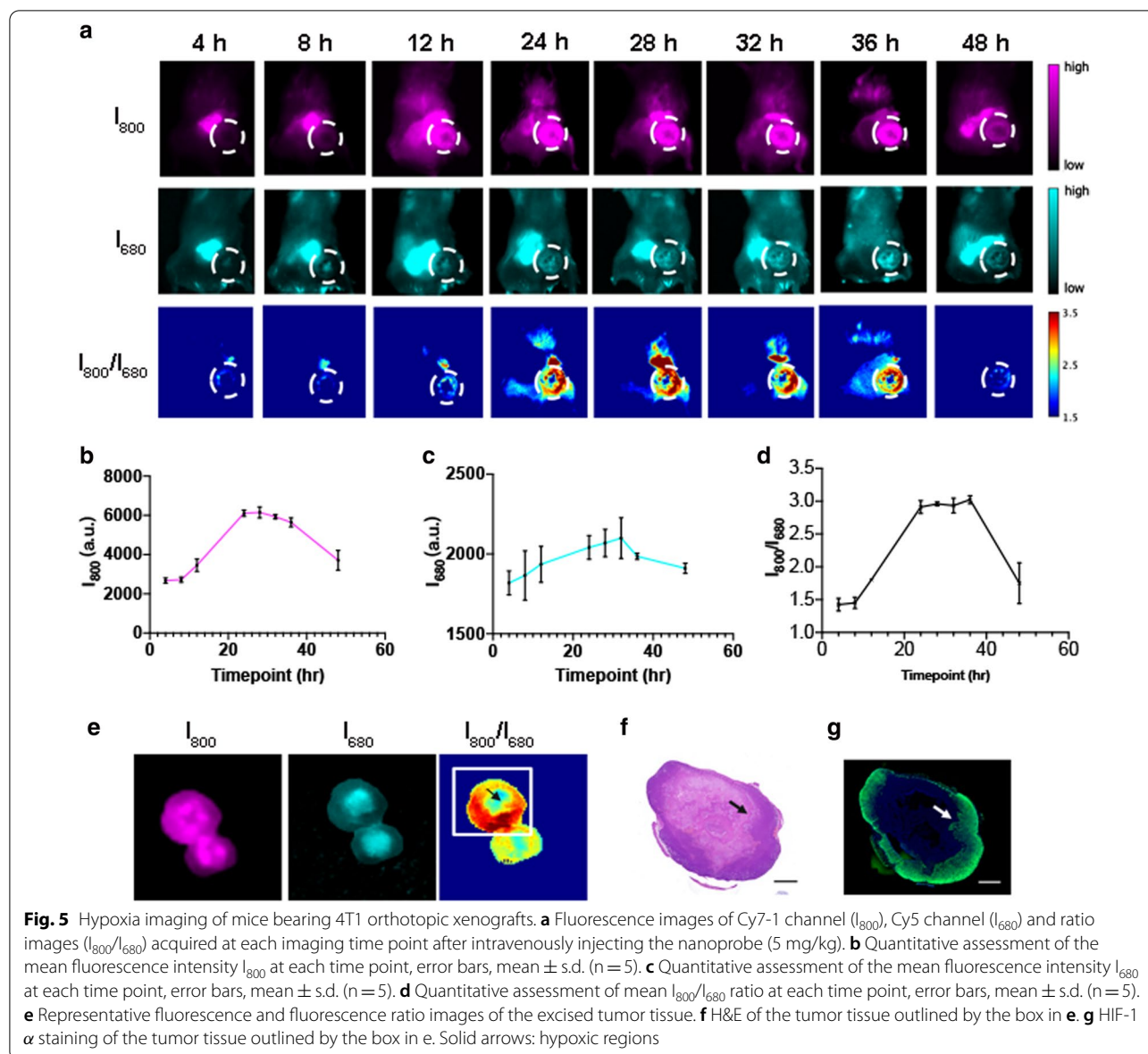
In vivo hypoxia imaging in orthotopic 4T1 tumor model

To investigate the feasibility of using Cy7-1/PG5-Cy5@LWHA to quantitatively assess tumor hypoxia in vivo, a mouse model bearing orthotopic 4T1 tumors was established. Tumors were allowed to grow for 4 weeks after inoculation to develop hypoxic conditions. For in vivo imaging, 200 μ l Cy7-1/PG5-Cy5@LWHA (1 mg/ml) was administered intravenously and mice were imaged at 4, 8, 12, 24, 28, 32, 36, and 48 h post injection. Fluorescence images of Cy7-1 (I_{800}), Cy5 (I_{680}), and ratio images (I_{800}/I_{680}) of a representative case are shown in Fig. 5a. Signals were detected in the tumor region (white dashed circle) starting from 12 h post injection, demonstrating the long circulation time of the nanoprobe and its gradual accumulation in the tumor area. Ratio images taken between 24 and 36 h distinctively outlined the tumor, indicating the successful activation



of the nanoprobe. Quantitative analysis of five mice confirmed that both I_{800} and I_{680} started to increase at 12 h, reached a plateau at 24 h, and remained stable up to 36 h, before diminishing at 48 h post injection (Fig. 5b, c). Similarly, the I_{800}/I_{680} ratio remained stable between 24 and 36 h post injection (Fig. 5d), which provides a flexible window for hypoxia assessment.

To further explore the proposed ratiometric imaging in ex vivo tissue, mice were euthanized after in vivo imaging and the tumors were dissected, split from the middle, and imaged. Representative images are shown in Fig. 5e. The I_{800}/I_{680} image showed heterogeneous signal distribution within the tumor, representing the spatial distribution of hypoxia. To verify this ex vivo



findings, hematoxylin and eosin (H&E) histopathology and immunofluorescence (IF) analysis of HIF-1 α were performed to examine the tissue composition and hypoxia distribution. Representative pathology images of the tumor section outlined in Fig. 5e (white box) are presented. Indeed, the peripheral tissue region with higher I_{800}/I_{680} ratio (solid arrows) correlated with the HIF-1 α -positive area in the IF image (Fig. 5g, green). The central region with low I_{800}/I_{680} and low HIF-1 α expression was mainly the necrotic tissue. Therefore, ratiometric imaging of Cy7-1/PG5-Cy5@LWHA successfully highlighted the hypoxic tumors in vivo, and precisely delineated the spatial distribution of hypoxia in the ex vivo tissue.

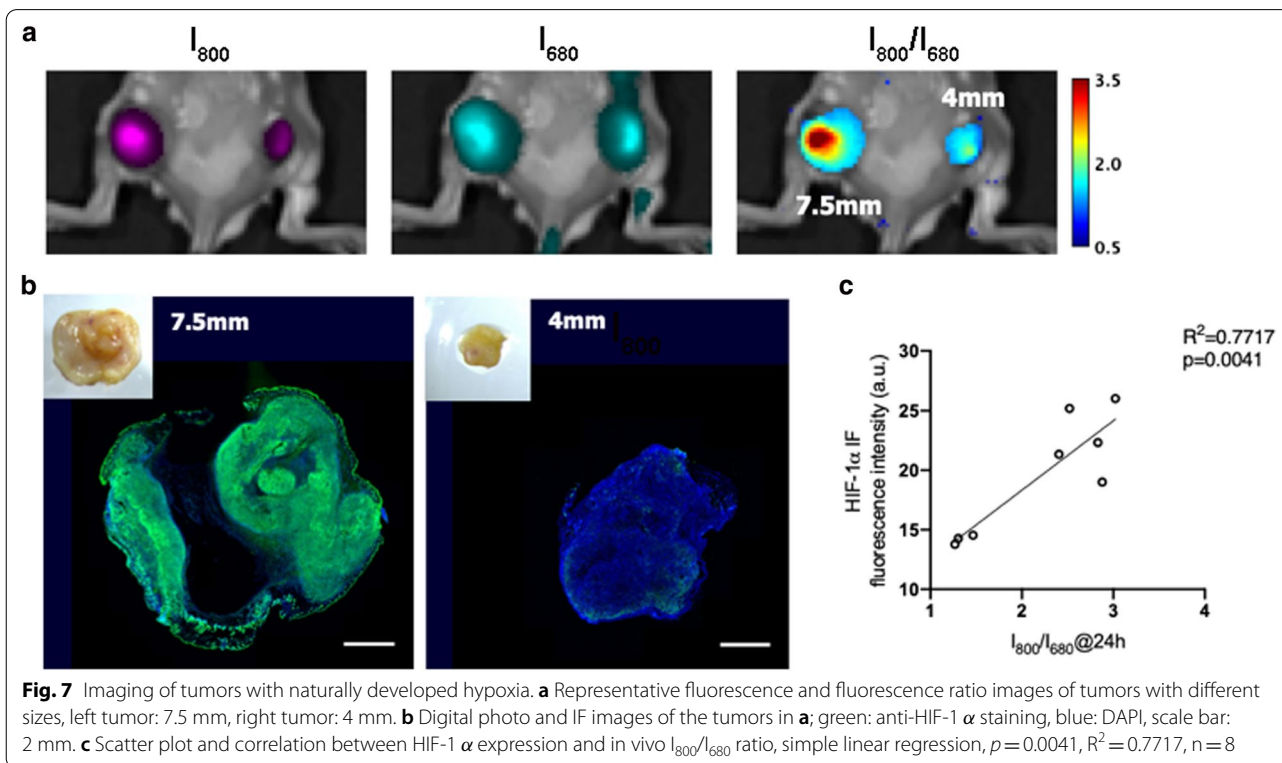
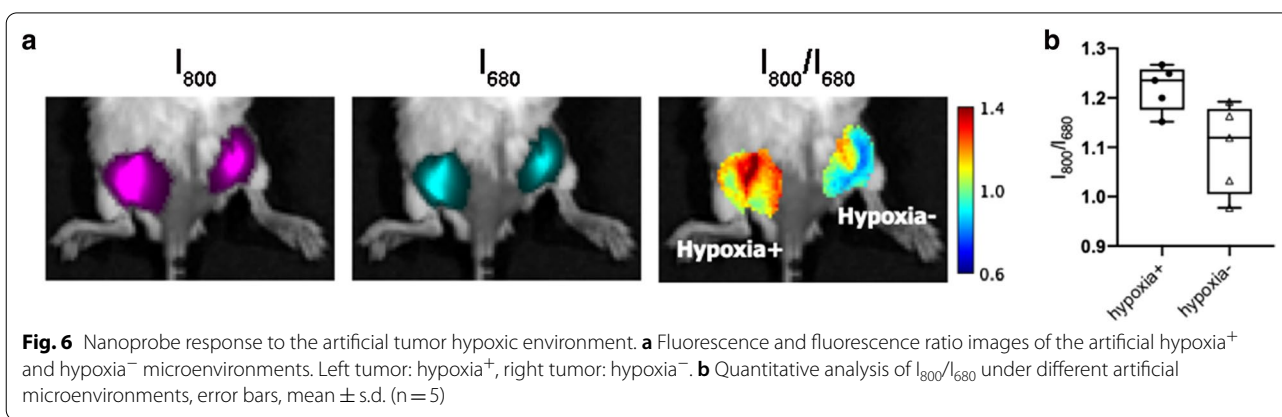
Quantitative imaging of tumors with different hypoxic levels

To explore whether the developed imaging approach could differentiate hypoxic and normoxic tumors in vivo, we again used CoCl₂-treated 4T1 cells to create an artificial hypoxic microenvironment [26]. Cells cultured under regular conditions were used as normoxic controls. The same number of hypoxia⁺ and hypoxia⁻ cells (10⁶) were mixed with the nanoprobe (0.1 mg/ml, 100 μ l) and injected into the left and right flanks of BALB/c mice. In vivo images were acquired 4 h after injection. As shown in Fig. 6a, the signal difference between hypoxia⁺ and hypoxia⁻ tumors was not evident in either Cy7-1 (I_{800}) or Cy5 (I_{680}) fluorescence images. However, in the

I_{800}/I_{680} ratio image, hypoxia⁺ tumor on the left exhibited a higher signal than the hypoxia⁻ control. Quantitative analysis of five mice demonstrated that the average I_{800}/I_{680} ratio of hypoxia⁺ tumors was ~11% higher than that of the hypoxia⁻ tumors (Fig. 6b).

To further validate the imaging strategy in a more clinically relevant setting, we established subcutaneous 4T1 tumors of different sizes on the bilateral flanks of BALB/c mice, representing a serial stage of naturally developed hypoxic tumors. We assumed that tumors with larger sizes would exhibit more severe hypoxia. For in vivo imaging, mice were intravenously injected with

the nanoprobe and imaged with the IVIS system 24 h post injection. Similar to the results presented in Fig. 5, the fluorescence of both Cy5 (I_{680}) and Cy7-1 (I_{800}) could be observed in the tumor area, indicating the accumulation of the nanoprobe regardless of the tumor size. In the example shown in Fig. 7a, the left and right tumors exhibited comparable Cy5 fluorescence (I_{680}), while the larger tumor (left flank, 7.5 mm) showed notably higher Cy7-1 fluorescence (I_{800}) than the smaller tumor (right flank, 4 mm). In the I_{800}/I_{680} ratio image, the signal from the 7.5 mm tumor appeared to be significantly higher than that from the 4 mm tumor, indicating a higher



degree of hypoxia. The hypoxic status of the tumors was further confirmed by IF staining against HIF-1 α . As shown in Fig. 7b, the 7.5 mm tumor exhibited much higher HIF-1 α expression than the 4 mm tumor, in consistent with the in vivo imaging result. Unlike the orthotopic tumors (Fig. 5), the subcutaneous tumors display a hypoxic gradient with stronger signal in the center of the tumor, which can be observed from both the in vivo ratio images and the ex vivo IF images. We believe that the different vasculature and microenvironment in different tumor models contribute to the distinctive hypoxia gradient. To further investigate the reliability of our imaging approach to quantify the hypoxic status, in vivo I_{800}/I_{680} ratio was compared with the ex vivo IF result. As presented in Fig. 7c, HIF-1 α expression level quantified from IF showed a significant correlation with the I_{800}/I_{680} ratio from in vivo imaging, with $R^2 = 0.7717$ and $p < 0.005$.

Detection of lymph node metastasis using ratiometric hypoxia imaging

The microenvironment in the primary tumor can be very different from that in the metastatic site. Nevertheless, it has been discovered that the hypoxic profile of the primary tumor could be preserved in metastatic lesions [6]. Therefore, we hypothesized that elevated NTR activity would be a biomarker for detecting lymph node (LN) metastasis. To test our hypothesis, the LN metastasis mouse model was established by injecting 4T1-GFP

breast cancer cells into the footpad of BALB/c nude mice. Three weeks after tumor inoculation, subcutaneous tumor can be observed in the footpad and enlarged popliteal LN (pLN) was palpable. For LN imaging, 1 mg/ml Cy7-1/PG5-Cy5@LWHA was injected intratumorally. The pLN on the opposite side was used as a control, and the same amount of nanoprobe was administered through footpad injection. Fluorescence images were acquired 3 h post injection. As shown in Fig. 8a, the nanoprobe was able to migrate to the pLNs, as revealed by the I_{680} fluorescence image. The tumor-associated pLN exhibited higher I_{680} signal intensity as compared to the control pLN, indicating more probe accumulation in the tumor-associated pLN. As a result, I_{800} or I_{680} image alone could not reveal the metastatic status of the node, since signal enhancement could either result from probe accumulation or elevated NTR activity. On the other hand, I_{800}/I_{680} image rectified the concentration effect, highlighting the tumor-associated pLN. After imaging, LNs were excised and imaged under the same condition. Ex vivo imaging results were comparable to those of in vivo imaging, as shown in Fig. 8b. To verify the imaging findings, the LNs were cryosectioned and scanned with a fluorescence microscope. As shown in Fig. 8c, 4T1 cancer cells exhibiting GFP fluorescence (arrows) can be identified in the tumor-associated pLN, confirming the metastatic status. Furthermore, since the GFP gene is solely expressed by 4T1-GFP cells, GFP expression was

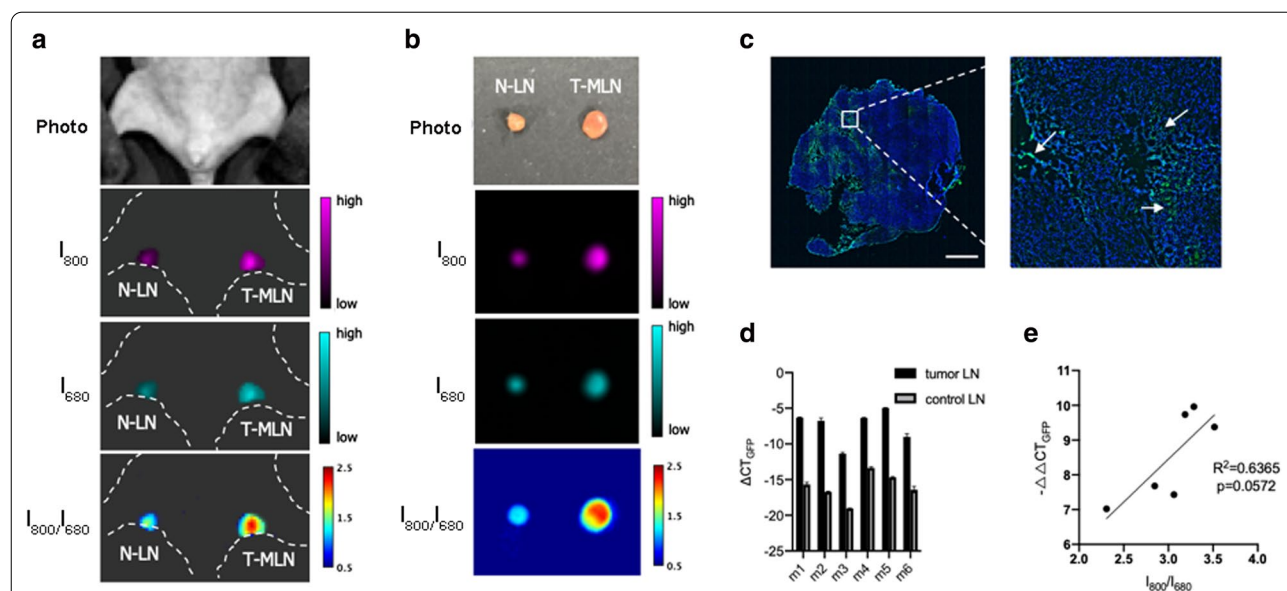


Fig. 8 Imaging of lymph-node metastasis. **a** Digital photo, in vivo fluorescence and fluorescence ratio images of tumor-associated pLN and control pLN. **b** Digital photo, ex vivo fluorescence and fluorescence ratio images of the excised pLNs. **c** GFP fluorescence image confirming the presence of metastatic 4T1-GFP cells in the tumor-associated pLN; solid arrows: GFP fluorescence tumor cells. **d** qPCR showing the relative expression of GFP in the control and tumor-draining pLNs of each mouse, error bar, mean \pm s.d. (n = 6). **e** Linear regression determined the correlation between in vivo imaging and qPCR results ($R^2 = 0.6365$, $p = 0.0572$)

determined using qPCR to evaluate the tumor burden in the nodes. The relative GFP expression was determined using the equation $\Delta CT = CT_{GAPDH} - CT_{GFP}$, where CT_{GAPDH} and CT_{GFP} are the cycle threshold of the GAPDH (internal control) and GFP genes, respectively. As shown in Fig. 8d, relative GFP expression in the metastatic LNs were distinctively higher than the control LN in all 6 mice. However, the GFP expression was slightly different among individual mice, suggesting different tumor burden in the metastatic nodes. Since NTR activity is an endogenous property of tumor cells, we further investigated whether I_{800}/I_{680} ratio of Cy7-1/PG5-Cy5@LWHA could reflect the amount of tumor cells in the LNs. For each mouse, tumor burden was determined using the equation $\Delta\Delta CT = \Delta CT_{T-MLN} - \Delta CT_{N-LN}$, where ΔCT_{T-MLN} and ΔCT_{N-LN} are the cycle threshold of the tumor metastatic LN and normal LN, respectively. As shown in Fig. 8e, in vivo I_{800}/I_{680} showed a good linear correlation with the tumor burden in the metastatic nodes, with $R^2 = 0.6365$ and $p = 0.0572$. To this end, we demonstrated the feasibility of using ratiometric imaging of Cy7-1/PG5-Cy5@LWHA to identify metastatic LNs in vivo. Quantitative imaging also allowed for tumor burden estimation with accuracy comparable to that of qPCR.

Discussion

Activatable molecular probes have gained significant interest in recent years because of their superior sensitivity and specificity (in comparison with traditional “always-on” probes) [27]. Small-molecule probes that can be activated by hypoxia, pH, ROS, and enzymes have been developed for tumor imaging [13–17, 28–31]. However, the in vivo use of activatable probes with single fluorescence emission remains challenging. Although most of the activatable probes were delicately designed to exhibit linear signal dependency on the concentration of the targeted analytes, few were able to provide quantitative information reliably in vivo.

This problem is especially prominent in hypoxia imaging, as regions with severe hypoxia are often affected by higher levels of vascular abnormalities and limited probe delivery [18]. In this study, we developed a dual-emission activatable nanoprobe, Cy7-1/PG5-Cy5@LWHA, which allows for self-calibration and quantitative hypoxia imaging. Our results show that the proposed imaging approach can accurately differentiate tumors with different hypoxic levels, which provides a novel imaging technique for evaluating hypoxia in vivo. This ratiometric approach and dual-emission probe design can be easily used with different applications by simply replacing Cy7-1 with another activatable dye. In this study, Cy5 was used as the “always-on” fluorophore because its

fluorescence spectrum can be easily separated from that of Cy7-1. Future studies may introduce NIR-II fluorophores as an internal reference with lower interference in tissue scattering [32].

In addition, our results showed that hypoxia imaging successfully identified the metastatic LNs. Previous studies have shown that the hypoxia signatures of the primary tumor may be preserved at the metastatic site [6]. Our results suggest that elevated NTR activity is a hypoxia signature that could be used as an imaging target for LN metastasis. A common problem in LN mapping is that tumor growth in the LNs alters the interstitial pressure and lymph flow rates, leading to heterogeneous probe delivery. As a result, the metastatic status of the LN could not be reliably determined using single-emission probes. To address this problem, previous studies have used a dual tracer approach, simultaneously using targeted and untargeted probes, to eliminate the concentration effect [33]. However, the two tracers need to have identical pharmacokinetics but different target affinities, which is very demanding in terms of probe design and synthesis, as both probes need to have the same molecular weight, size, and zeta potential. In our system, we coupled hypoxia-activatable and “always-on” fluorophores using a nanocarrier, to ensure identical pharmacokinetics. The “always-on” Cy5 fluorescence helped to track the LNs in the tumor region, and the ratio between the hypoxia-activatable signal and the “always-on” signal enabled quantitative identification of the metastatic nodes. This information could potentially assist clinical decision-making during surgery to locate and diagnose metastatic LNs in real time.

Conclusion

Overall, this study developed a novel imaging strategy combining a self-calibrated activatable nanoprobe with ratiometric image analysis, for the quantitative assessment of tumor hypoxia in vivo. Using this strategy, dynamic changes of hypoxia during tumor growth could be monitored in vivo in real time. The successful detection of metastatic LNs presented in this work further validated the potential clinical translation of this imaging strategy.

Materials and methods

Probe Synthesis and Characterization

Cy5-NHS (146368-14-1, RuixiBio, Shaanxi, China) was first labeled with PG5 (536709, Sigma-Aldrich, St. Louis MA, USA) to form PG5-Cy5. Briefly, 300 mg of PG5 was dissolved in 5 ml of borate buffer (pH 9.0). To this solution, Cy5-NHS (3 mg) prepared in DMF was added and stirred for 24 h at room temperature in the dark. The reaction product was then transferred into a 5 K MWCO

dialysis bag (YA1058, Solarbio, Beijing, China) and dialyzed against ddH₂O for two days. Purified PG5-Cy5 was retrieved by freeze-drying. Cy7-1 was synthesized in accordance with a previously reported protocol [18]. To encapsulate Cy7-1 in the interior of PG5-Cy5, 2 mg Cy7-1 was dissolved in acetone (200 μ l) and slowly added to PG5-Cy5 (4 mg) in ddH₂O (8 ml). After stirring on ice for 2 h, the mixture was transferred to a 10 kDa ultrafiltration tube (UFC801096, Millipore, Burlington, MA, USA) and centrifuged at 5500 rpm for 15 min at 4 °C. Subsequently, Cy7-1/PG5-Cy5 was functionalized with LWHA (R-HC-5 K, RuixiBio, Shaanxi, China). Cy7-1/PG5-Cy5 was mixed with LWHA at a mass ratio of 1:1 in ddH₂O. The mixture was vortexed for 30 s and incubated at 4 °C for 1 h. Finally, the reaction product was dialyzed against ddH₂O overnight to obtain purified Cy7-1/PG5-Cy5@LWHA. To confirm the successful synthesis of the nanoprobe, absorption and fluorescence spectra were measured after each synthesis step. Absorption spectra were measured on a spectrophotometer (UV-3600Plus, Shimadzu, Kyoto, Japan), and fluorescence spectra were measured using a fluorometer (F-7000, Hitachi, Tokyo, Japan). The hydrodynamic size and zeta potential were measured using a Dynamic Light Scattering Zetasizer (Nano-ZS90, Malvern Instruments, Malvern, UK). The size and morphology of the nanoprobe were observed by TEM (JEM 1200EX, Jeol, Tokyo, Japan). The composition of the nanoprobe was characterized by Fourier transform infrared spectroscopy (Nicolet iS10, Thermo Fisher Scientific, Waltham, MA, USA).

Probe response to NTR in vitro

To verify the probe's response to NTR, 0.25 mg/ml Cy7-1/PG5-Cy5@LWHA in Tris buffer was mixed with 500 μ M NADH (N8129, Sigma-Aldrich, St. Louis, MA, USA) and 0.5 μ g/ml NTR (N9284, Sigma-Aldrich, St. Louis, MA, USA). The solution was incubated at 37 °C for 10 min. The fluorescence spectra of the nanoprobe were recorded before and after the reaction. To show the ratiometric imaging performance of the probe, Cy7-1/PG5-Cy5@LWHA, NADH, and NTR were mixed in 96-well plates, incubated at 37 °C for 10 min, and imaged using an IVIS imaging system (PerkinElmer, Waltham, MA, USA). Nanoprobe concentrations were modulated from 0 to 0.29 mg/ml and NTR concentrations ranging from 0 to 1.5 μ g/ml were used. Cy5 was excited at 640 nm and emission was recorded at 680 nm. Cy7-1 was excited at 745 nm and emission was recorded at 800 nm. Regions of interest (ROIs) were selected to include the area of each well. The mean fluorescence intensities of Cy7-1 (I_{800}) and Cy5 (I_{680}) were generated for each ROI in ImageJ. The I_{800}/I_{680} ratio was calculated and the I_{800}/I_{680}

vs. NTR concentration curve was plotted for each probe concentration.

Cell culture and in vitro imaging

Mouse breast cancer cell lines 4T1 and 4T1 transfected with Green fluorescence protein (4T1-GFP) genes were grown in RPMI-1640 medium (Gibco, Waltham, MA, USA) supplemented with 10% fetal bovine serum (Gibco, Waltham, MA, USA). Cells were cultured in a humidified atmosphere containing 5% CO₂ at 37 °C. To induce hypoxia in cell culture, 4T1-GFP cells were incubated with 70 μ M CoCl₂ (Macklin, Shanghai, China) in serum-free RPMI medium overnight. For confocal imaging, cells were seeded at a density of 50,000 cells in 35 mm glass-bottomed imaging dishes (Biosharp, Hefei, China) and cultured overnight. Prior to imaging, cells were incubated with the nanoprobe (0.05 mg/ml) for 4 h and washed three times with PBS (Gibco, Waltham, MA, USA). Cells were then incubated with 2 μ g/ml DAPI (Solarbio, Beijing, China) for 20 min to label the nuclei. To block CD44, cells were first incubated with 0.05 mg/ml LWHA for 2 h. In vitro imaging was performed using a confocal microscope (Andor Dragonfly, Oxford Instruments, Abingdon, UK) with a 40 \times objective. For the Cy5 and Cy7-1 channels, cells were excited at 637 nm and 730 nm, respectively.

Cytotoxicity test

Cytotoxicity was evaluated using the MTT cell proliferation and cytotoxicity assay kit (M1020, Solarbio). 4T1 cells were seeded in 96-well plates and cultured overnight in a humidified atmosphere containing 5% CO₂ at 37 °C. After monolayer formation, different concentrations of the nanoprobe (0, 1, 2, 10, 50 and 100 μ g/ml) were added to the cells and incubated for 4 h. After incubation, the cells were washed with PBS and 90 μ l RPMI-1640 medium and 10 μ l MTT solution were added to each well and incubated with the cells for another 4 h. Afterward, the supernatant was discarded and 110 μ l formazan was added to each well. The plates were gently shaken for 10 min. The OD₄₉₀ of each well was measured using a microplate reader (Biotek, Winooski, VT, USA).

In vivo imaging of orthotopic tumor model

Following ethical approval No. IA-202105, all animal experiments were performed in compliance with the guidelines set by the Animal Care Committee at the Institute of Automation, Chinese Academy of Science (license #SYXK(京) 2020-0049). To establish the orthotopic breast tumor model, 4T1 cells (1×10^6 cells in 100 μ l PBS) were injected into the 4th inguinal mammary fat pad of female BALB/c mice (6 weeks old, Charles River).

Tumor growth was monitored for 3–4 weeks post inoculation. Once the tumor size reached 5–10 mm, 200 μ l Cy7-1/PG5-Cy5@LWHA nanoprobe (1 mg/ml in PBS) was injected into the mice via the tail vein. Mice were imaged at 4, 8, 12, 24, 28, 32, 36, and 48 h post injection using the IVIS imaging system. The image settings for Cy5 and Cy7-1 were the same as those described above. At 48 h post injection, the mice were sacrificed, and the tumor and major organs were collected and imaged using an IVIS imaging system.

In vivo imaging of artificial hypoxic microenvironment

To establish an artificial hypoxic tumor microenvironment, 4T1 cells were incubated with 70 μ M CoCl₂ in serum-free RPMI medium overnight. Hypoxic cells were collected and resuspended in PBS at a density of 1×10^7 cells/ml. Hundred microliter of cell suspension was mixed with 100 μ l Cy7-1/PG5-Cy5@LWHA nanoprobe (0.1 mg/ml) and subcutaneously injected into the right flank of female BALB/c mice. As a normoxic control, the same number of 4T1 cells cultured under regular conditions were mixed with Cy7-1/PG5-Cy5@LWHA and injected into the left flank of the same mouse. Mice were imaged with an IVIS imaging system 4 h post injection.

In vivo imaging of tumors with different hypoxic status

To investigate the ability of the nanoprobe to quantify tumor hypoxic status, subcutaneous 4T1 tumors of different sizes were established on the flanks of female BALB/c mice. In each mouse, two tumors were grown on the bilateral flanks. The first tumor was implanted on the left flank by subcutaneous injection of 1×10^6 4T1 cells. Once it reached a palpable size at 10 days post inoculation, a second tumor was similarly established in the right flank. Ten days after the second inoculation, two tumors of different sizes were established. For in vivo imaging, mice were intravenously injected with 200 μ l of Cy7-1/PG5-Cy5@LWHA (1 mg/ml) and imaged with the IVIS imaging system 24 h post injection.

In vivo imaging of metastatic LN

To establish LN metastasis of 4T1 breast cancer cells, 1×10^5 4T1-GFP cells resuspended in 30 μ l PBS were injected into the left footpad of Balb/c nude mice. Tumor growth was monitored for 3 weeks until a palpable pLN was observed. For in vivo imaging, 30 μ l of Cy7-1/PG5-Cy5@LWHA nanoprobe (1 mg/ml) was injected intratumorally into the left footpad. The same amount of nanoprobe was injected into the right footpad as a control. In vivo images of LN were acquired using the IVIS imaging system at 3 h post injection.

Ratiometric processing and hypoxia quantification

Pixel-based ratio images were generated in ImageJ 1.53a according to the following equation:

$$\frac{I_{800}}{I_{680}} = \begin{cases} \text{NAN, if } I_{800ij} < p \text{ OR } I_{680ij} < q, \\ \frac{I_{800}}{I_{680}} \text{ if } I_{800ij} \geq p \text{ AND } I_{680ij} \geq q \end{cases}$$

where i and j denote the pixel coordinates, I_{800} was the pixel value of the Cy7-1 fluorescence image, I_{680} is the pixel value of the Cy5 fluorescence image, p is the threshold value chosen to remove the background in the Cy7-1 fluorescence image, q is the threshold value chosen to remove the background in the Cy5 fluorescence image. To obtain the ratio information of a certain area, the ROI was selected, and the average value $\frac{I_{800}}{I_{680 \text{ ave}}}$ was calculated. For all computations, images were converted to 32-bit and processed.

Histological evaluation

Excised tissue was fixed in 10% formalin and embedded in paraffin; 4 μ m-thick sections were sectioned with a microtome and stained with H&E. Immunofluorescence was used to evaluate HIF-1 α expression. The antibodies and staining reagents used were anti-HIF-1 α (ab228649, Abcam, Cambridge, UK), 488-conjugated goat anti-rabbit IgG (GB25303, Servicebio, Wuhan, China), and DAPI (G1020, Servicebio, Wuhan, China). Immunofluorescence was performed according to an established protocol (www.abcam.com/protocols). H&E and fluorescence images were acquired using a Panoramic MIDI scanner (3DHISTECH).

qPCR

GFP expression was analyzed to evaluate the tumor burden in metastatic LNs. Briefly, LNs were excised and freshly frozen in RNAlater reagent (SR0020, Solarbio, Beijing, China). Total RNA was isolated according to the protocol provided in www.abcam.com/protocols. To assess gene expression, cDNA was prepared using the Servicebio[®] RT First Strand cDNA Synthesis Kit (G3330, Servicebio, Wuhan, China). Fifteen microliter reaction was set up using 7.5 μ l 2 \times SYBR Green qPCR Master Mix (G3320, Servicebio, Wuhan, China), 2.5 μ M primer forward (GFP: GGGACCGCTCCTTCCTGTT, GAPDH: CCTCGTCCCGTAGACAAAATG) and primer reverse (GFP: ACGGGGATGATCTTCTCGCA, GAPDH: TGA GGTCAATGAAGGGGTCGT), 2.0 μ l cDNA template and 4 μ l ddH₂O. qPCR was performed using the CFX96 Touch Real-Time PCR Detection System (Bio-Rad, Hercules, CA, USA). Each sample was tested in triplicate. GAPDH was used as an endogenous control. The

relative GFP gene expression level was determined using $\Delta CT = CT_{GAPDH} - CT_{GFP}$, where CT is the threshold cycle. The tumor burden in the metastatic LNs was represented by $\Delta\Delta CT = \Delta CT_{T-MLN} - \Delta CT_{N-LN}$.

Statistical analysis

Data analysis was performed using GraphPad Prism ver. 9. For in vitro imaging experiments, an unpaired t -test with Welch's correction was used to determine the statistical difference. For in vivo imaging experiments, the Wilcoxon matched-pairs signed rank test was used to determine the differences between different hypoxia groups. Simple linear regression was used to compare ex vivo HIF-1 α expression with in vivo I_{800}/I_{680} at 24 h, and to compare tumor burden determined from $\Delta\Delta CT$ of qPCR with in vivo I_{800}/I_{680} in tumor-draining LNs. All data are presented as mean \pm s.d. Statistical significance was set at $p < 0.05$.

Abbreviations

CT: Cycle threshold; HIF-1: Hypoxia-inducible transcription factor; H&E: Hematoxylin and eosin; IF: Immunofluorescence; LWHA: Low molecular weight hyaluronic acid; LN: Lymph node; NTR: Nitroreductase; PG5: Poly(amidoamine) dendrimer, 5th generation; TEM: Transmission electron microscopy.

Supplementary Information

The online version contains supplementary material available at <https://doi.org/10.1186/s12951-022-01341-9>.

Additional file 1: Figure S1. FTIR spectrum of Cy7/PG5-Cy5@LWHA.

Additional file 2: Figure S2. NTR response of free Cy7-1.

Additional file 3: Figure S3. Cytotoxicity of (a) Cy7-1/PG5-Cy5@LWHA and (b) Cy7-1/PG5-Cy5.

Acknowledgements

The authors would like to acknowledge the instrumental and technical support of Multimodal Biomedical Imaging Experimental Platform, Institute of Automation, Chinese Academy of Sciences.

Authors' contributions

XF and CL designed and fabricated the nanoprobe. XF and SZ performed the cell and animal experiments. YL designed and fabricated the activatable Cy7-1 probe. XF performed the data analysis and drafted the manuscript. JT oversaw the entire experimental design and did the critical revision of the manuscript. All authors read and approved the final manuscript.

Funding

This paper is supported by Ministry of Science and Technology of China under Grant No. 2017YFA0205200, 2017YFC1309100, National Natural Science Foundation of China under Grant No. 62027901, 81227901, 81930053, 82093219055, Natural Science Foundation of Beijing, China under Grant No. 7212207, The State Key Laboratory of Management and Control for Complex Systems, Institute of Automation, Chinese Academy of Sciences under Grant No. 2021QN02, The Project of High-Level Talents Team Introduction in Zhuhai City (Zhuhai HLHPTP201703).

Availability and data and materials

All data required to reproduce the results can be obtained from the corresponding author upon request.

Declarations

Ethics approval and consent to participate

Following ethical approval No. IA-202105, all animal experiments were performed in compliance with the guidelines set by the Animal Care Committee at the Institute of Automation, Chinese Academy of Science (license #SYXK(京) 2020-0049).

Consent for publication

All authors agree to be published.

Competing interests

The authors have no conflict of interest.

Author details

¹CAS Key Laboratory of Molecular Imaging, Beijing Key Laboratory of Molecular Imaging, the State Key Laboratory of Management and Control for Complex Systems, Institute of Automation, Chinese Academy of Sciences, Beijing 100190, China. ²School of Artificial Intelligence, University of Chinese Academy of Science, Beijing 100080, China. ³Institute of Bismuth Science and School of Materials and Chemistry, University of Shanghai for Science and Technology, Shanghai 200093, China. ⁴Beijing Advanced Innovation Center for Big Data-Based Precision Medicine, School of Medicine and Engineering, Beihang University, Beijing 100191, China. ⁵Engineering Research Center of Molecular and Neuro Imaging of Ministry of Education, School of Life Science and Technology, Xidian University, Xi'an, Shaanxi 710126, China. ⁶Key Laboratory of Big Data-Based Precision Medicine (Beihang University), Ministry of Industry and Information Technology, Beijing 100191, China.

Received: 26 January 2022 Accepted: 1 March 2022

Published online: 18 March 2022

References

- Denko NC. Hypoxia, HIF1 and glucose metabolism in the solid tumour. *Nat Rev Cancer*. 2008;8(9):705–13.
- Papandreou I, Cairns RA, Fontana L, Lim AL, Denko NC. HIF-1 mediates adaptation to hypoxia by actively downregulating mitochondrial oxygen consumption. *Cell Metab*. 2006;3(3):187–97.
- Gilkes DM, Semenza GL, Wirtz D. Hypoxia and the extracellular matrix: drivers of tumour metastasis. *Nat Rev Cancer*. 2014;14(6):430–9.
- Montagner M, Enzo E, Forcato M, Zanconato F, Parenti A, Rampazzo E, Basso G, Leo G, Rosato A, Bicciato S, et al. SHARP1 suppresses breast cancer metastasis by promoting degradation of hypoxia-inducible factors. *Nature*. 2012;487(7407):380–4.
- Rankin EB, Giaccia AJ. Hypoxic control of metastasis. *Science*. 2016;352(6282):175–80.
- Godet I, Shin YJ, Ju JA, Ye IC, Wang G, Gilkes DM. Fate-mapping post-hypoxic tumor cells reveals a ROS-resistant phenotype that promotes metastasis. *Nat Commun*. 2019;10(1):4862.
- Ebright RY, Zachariah MA, Micalizzi DS, Wittner BS, Niederhoffer KL, Nieman LT, Chirn B, Wiley DF, Wesley B, Show B, et al. HIF1A signaling selectively supports proliferation of breast cancer in the brain. *Nat Commun*. 2020;11(1):6311.
- Li Z, Li X, Gao X, Zhang Y, Shi W, Ma H. Nitroreductase detection and hypoxic tumor cell imaging by a designed sensitive and selective fluorescent probe, 7-[(5-nitrofuranyl)methoxy]-3H-phenoxazin-3-one. *Anal Chem*. 2013;85(8):3926–32.
- Fan Y, Lu M, Yu X, He M, Zhang Y, Ma X, Kou J, Yu B, Tian J. Targeted myocardial hypoxia imaging using a nitroreductase-activatable near-infrared fluorescent nanoprobe. *Anal Chem*. 2019;91(10):6585–92.
- Liu Y, Zhang L, Nazare M, Yao Q, Hu HY. A novel nitroreductase-enhanced MRI contrast agent and its potential application in bacterial imaging. *Acta Pharm Sin B*. 2018;8(3):401–8.
- Pitsawong W, Hoben JP, Miller AF. Understanding the broad substrate repertoire of nitroreductase based on its kinetic mechanism. *J Biol Chem*. 2014;289(22):15203–14.

12. Jiao Y, Zhang L, Gao X, Si W, Duan C. A cofactor-substrate-based supra-molecular fluorescent probe for the ultrafast detection of nitroreductase under hypoxic conditions. *Angew Chem Int Ed Engl.* 2020;59(15):6021–7.
13. Geng WC, Jia S, Zheng Z, Li Z, Ding D, Guo DS. A noncovalent fluorescence turn-on strategy for hypoxia imaging. *Angew Chem Int Ed Engl.* 2019;58(8):2377–81.
14. Zheng X, Wang X, Mao H, Wu W, Liu B, Jiang X. Hypoxia-specific ultrasensitive detection of tumours and cancer cells in vivo. *Nat Commun.* 2015;6:5834.
15. Li Y, Sun Y, Li J, Su Q, Yuan W, Dai Y, Han C, Wang Q, Feng W, Li F. Ultrasensitive near-infrared fluorescence-enhanced probe for in vivo nitroreductase imaging. *J Am Chem Soc.* 2015;137(19):6407–16.
16. Zheng J, Shen Y, Xu Z, Yuan Z, He Y, Wei C, Er M, Yin J, Chen H. Near-infrared off-on fluorescence probe activated by NTR for in vivo hypoxia imaging. *Biosens Bioelectron.* 2018;11(9):141–8.
17. Liu F, Zhang H, Li K, Xie Y, Li Z. A novel NIR fluorescent probe for highly selective detection of nitroreductase and hypoxic-tumor-cell imaging. *Molecules.* 2021;26(15):4425.
18. Martin JD, Seano G, Jain RK. Normalizing function of tumor vessels: progress, opportunities, and challenges. *Annu Rev Physiol.* 2019;81:505–34.
19. Zhu D, Li Y, Zhang Z, Xue Z, Hua Z, Luo X, Zhao T, Lu C, Liu Y. Recent advances of nanotechnology-based tumor vessel-targeting strategies. *J Nanobiotechnology.* 2021;19(1):435.
20. Song C, Shen M, Rodrigues J, Mignani S, Majoral JP, Shi X. Superstructured Poly(amidoamine) dendrimer-based nanoconstructs as platforms for cancer nanomedicine: a concise review. *Coord Chem Rev.* 2020;421:213463.
21. Dai Y, Yu X, Wei J, Zeng F, Li Y, Yang X, Luo Q, Zhang Z. Metastatic status of sentinel lymph nodes in breast cancer determined with photoacoustic microscopy via dual-targeting nanoparticles. *Light Sci Appl.* 2020;9:164.
22. Hirn S, Semmler-Behnke M, Schleh C, Wenk A, Lipka J, Schaffler M, Takenaka S, Moller W, Schmid G, Simon U, Kreyling WG. Particle size-dependent and surface charge-dependent biodistribution of gold nanoparticles after intravenous administration. *Eur J Pharm Biopharm.* 2011;77(3):407–16.
23. Kizaka-Kondoh S, Konse-Nagasawa H. Significance of nitroimidazole compounds and hypoxia-inducible factor-1 for imaging tumor hypoxia. *Cancer Sci.* 2009;100(8):1366–73.
24. Muñoz-Sánchez J, Cháñez-Cárdenas ME. The use of cobalt chloride as a chemical hypoxia model. *J Appl Toxicol.* 2019;39(4):556–70.
25. Liu Y, Bryantsev VS, Diallo MS, Goddard WA III. PAMAM dendrimers undergo pH responsive conformational changes without swelling. *J Am Chem Soc.* 2009;131(8):2798–9.
26. Zheng X, Mao H, Huo D, Wu W, Liu B, Jiang X. Successively activatable ultrasensitive probe for imaging tumour acidity and hypoxia. *Nat Biomed Eng.* 2017;1:0057.
27. Li J, Cheng F, Huang H, Li L, Zhu JJ. Nanomaterial-based activatable imaging probes: from design to biological applications. *Chem Soc Rev.* 2015;44(21):7855–80.
28. Miao Q, Lyu Y, Ding D, Pu K. Semiconducting oligomer nanoparticles as an activatable photoacoustic probe with amplified brightness for in vivo imaging of pH. *Adv Mater.* 2016;28(19):3662–8.
29. Yang Z, Dai Y, Yin C, Fan Q, Zhang W, Song J, Yu G, Tang W, Fan W, Yunng BC, et al. Activatable semiconducting theranostics: simultaneous generation and ratiometric photoacoustic imaging of reactive oxygen species in vivo. *Adv Mater.* 2018;30(23):e1707509.
30. Li Y, Xue C, Fang Z, Xu W, Xie H. In vivo visualization of γ -Glutamyl 594 transpeptidase activity with an activatable self-immobilizing near-infrared probe. *Anal Chem.* 2020;92(22):15017–24.
31. Chen JA, Pan H, Wang Z, Gao J, Tan J, Ouyang Z, Guo W, Gu X. Imaging of ovarian cancers using enzyme activatable probes with second near-infrared window emission. *Chem Commun (Camb).* 2020;56(18):2731–4.
32. Li C, Chen G, Zhang Y, Wu F, Wang Q. Advanced fluorescence imaging technology in the near-infrared-ii window for biomedical applications. *J Am Chem Soc.* 2020;142(35):14789–804.
33. Tichauer KM, Samkoe KS, Gunn JR, Kanick SC, Hoopes PJ, Barth RJ, Kaufman PA, Hasan T, Pogue BW. Microscopic lymph node tumor burden quantified by macroscopic dual-tracer molecular imaging. *Nat Med.* 2014;20(11):1348–53.

Publisher's Note

Springer Nature remains neutral with regard to jurisdictional claims in published maps and institutional affiliations.

Ready to submit your research? Choose BMC and benefit from:

- fast, convenient online submission
- thorough peer review by experienced researchers in your field
- rapid publication on acceptance
- support for research data, including large and complex data types
- gold Open Access which fosters wider collaboration and increased citations
- maximum visibility for your research: over 100M website views per year

At BMC, research is always in progress.

Learn more biomedcentral.com/submissions

